

# Linear Stability Analysis of Compressible Channel Flow with Porous Walls

Iman Rahbari<sup>\*,1</sup> and Carlo Scalo<sup>1</sup>

## Abstract

We have investigated the effects of permeable walls, modeled by linear acoustic impedance with zero reactance, on compressible channel flow via linear stability analysis (LSA). Base flow profiles are taken from impermeable isothermal-wall laminar and turbulent channel flow simulations at bulk Reynolds number,  $Re_b = 6900$  and Mach numbers,  $M_b = 0.2, 0.5, 0.85$ . For a sufficiently high value of permeability, two dominant modes are excited: a bulk pressure mode, causing symmetric expulsion and suction of mass from the porous walls (Mode 0); a standing-wave-like mode, with a pressure node at the centerline (Mode 1). In the case of turbulent mean flow profiles, both modes generate additional Reynolds shear stresses augmenting the (base) turbulent ones, but concentrated in the viscous sublayer region; the trajectories of the two modes in the complex phase velocity space follow each other very closely for values of wall permeability spanning two orders of magnitude, suggesting their coexistence. The transition from subcritical to supercritical permeability does not alter significantly the structure of the two modes for the range of wavenumbers investigated, suggesting that wall permeability simply accentuates pre-existing otherwise stable modes. Results from the present investigation will inform the design of new control strategies for compressible turbulent boundary layers based on more general impedance boundary conditions and high-fidelity numerical simulation.

## 1 Introduction

In the present work we investigate the effects of porous walls modeled with a Darcy-like boundary condition derived as a particular case of linear acoustic impedance

---

(\*) Corresponding author, e-mail: irahbari@purdue.edu. (1) School of Mechanical Engineering, Purdue University, West Lafayette, IN 47907-2045, USA.

boundary condition (IBC) with zero reactance. The latter can be directly written in the time domain as

$$p' = R v'_n \quad (1)$$

where  $R$  is the wall-impedance resistance, and  $p'$  and  $v'_n$  are the fluctuating pressure and the wall-normal component of the velocity at the boundary (positive if directed away from the fluid side), normalized with a base density and speed of sound (unitary dimensionless base impedance). The present investigation is limited to a classic Linear Stability Analysis (LSA) approach and is inspired by the hydro-acoustic instability observed by Scalo, Bodart, and Lele [22], who performed numerical simulations of compressible channel flow with a three-parameter impedance model [23]. The effective wall permeability is a broadband function of the frequency of wall-normal waves chosen so as to allow maximum transpiration only at frequency of the large-scale turbulent energy containing eddies. Despite the different nature of the imposed wall-impedance, the results shown in the present investigation provide a useful theoretical framework for hydro-acoustic instabilities and a guide for future investigations in the manipulation of compressible boundary layer turbulence.

The effects of porous walls on shear flows has been a topic of formidable research effort, especially in the low-Mach-number limit. Lekoudis [9] performed LSA of an incompressible boundary layer over two types of porous surfaces: one modeling a perforated surface over a large chamber (with stabilizing effects); the second one, modeling pores over independent cavities (with negligible effects). Jiménez et al. [14] performed channel flow simulations over active and passive porous walls observing the creation of large spanwise-coherent Kelvin-Helmholtz in the outer layer responsible for frictional drag increase; the near-wall turbulence production cycle was not found to be significantly altered [13]. More recently, Tilton and Cortelezzi [24] investigated channel flow coated with finite-thickness homogeneous porous slabs. Two new unstable wall modes were discovered, one symmetric and one anti-symmetric, originating from the left branch of eigenvalue spectrum. Similar results will be discussed in the context of the present analysis.

From the viscous fully compressible Navier-Stokes equations for an ideal gas Malik [19] derived the three-dimensional linearized perturbation equations to investigate the linear stability properties of flat plate boundary layers for freestream Mach numbers up to 10. Duck et al [6] performed a similar investigation in the case of viscous compressible Couette flow, revealing fundamental differences with respect to unbounded cases. Hu and Zhong [10, 11] investigated supersonic viscous Couette flow at finite Reynolds numbers finding two unstable acoustic inviscid modes when a region of locally supersonic flow, relative to the phase speed of the instability wave, is present. Their structure was deemed in agreement with two acoustic modes shown by Mack[17], which are sustained by the acoustic interaction between the walls and the sonic line. Malik and co-workers[18] have also used modal and non-modal stability to study the effect of viscosity stratification on the stability of compressible Couette flow. Energy transfer from mean flow to perturbations occurs at two locations: near the top wall and in the bulk of flow domain, associated with two different unstable modes. More recent efforts are focused on the transitional

hypersonic boundary layer stability [3, 25, 26, 5, 27], where porous walls are used as means to delay transition by absorbing.

The present work aims to establish an LSA-based theoretical framework to inform control strategies of fully developed wall-bounded compressible boundary layer turbulence over porous wall, inspired by the observations of Scalo et al. [22]. Validation against previous LSA studies is first presented, as well as the impermeable-wall laminar and turbulent channel flow data used as the flow in our LSA. Finally, the structure of the unstable modes triggered by the porous wall is discussed along with their predicted effect on the structure of near-wall turbulence.

## 2 Problem Formulation

The base velocity, density and temperature profiles for the present LSA investigations have been taken from laminar and turbulent numerical simulations of fully compressible impermeable isothermal-wall channel flow including previous works. All of the results reported here are normalized with the channel's half-width, the bulk density (constant for channel flow), and the speed of sound, temperature and dynamic viscosity at the wall.

### 2.1 Nonlinear Simulations

The fully nonlinear dimensionless governing equations for conservation of mass, momentum and total energy are, respectively,

$$\frac{\partial}{\partial t}(\rho) + \frac{\partial}{\partial x_j}(\rho u_j) = 0 \quad (2)$$

$$\frac{\partial}{\partial t}(\rho u_i) + \frac{\partial}{\partial x_j}(\rho u_i u_j) = -\frac{\partial}{\partial x_i} p + \frac{1}{Re_a} \frac{\partial}{\partial x_i}(\tau_{ij}) + f_1 \delta_{1i} \quad (3)$$

$$\frac{\partial}{\partial t}(\rho E) + \frac{\partial}{\partial x_j}[u_j(\rho E + p)] = \frac{1}{Re_a} \frac{\partial}{\partial x_j}(u_i \tau_{ij} + q_j) + f_1 u_1 \quad (4)$$

where  $x_1$ ,  $x_2$  and  $x_3$  (alternatively  $x$ ,  $y$ , and  $z$ ) are, respectively, the streamwise, wall-normal and spanwise coordinates,  $u_i$  the velocity components in those directions. Thermodynamic pressure, density and temperature are related by the equation of state  $p = \gamma^{-1} \rho T$ , where  $\gamma$  is the ratio of specific heats.  $E$  is the total energy per unit mass and  $Re_a$  the Reynolds number based on the channel's half-width and speed of sound at the wall temperature, which is related to the bulk Mach and Reynolds numbers via  $Re_b = M_b Re_a$ . The viscous stress tensor and conductive heat fluxes are

$$\tau_{ij} = 2\mu \left[ S_{ij} - \frac{1}{3} \frac{\partial u_m}{\partial x_m} \delta_{ij} \right], \quad q_j = \frac{1}{\gamma-1} \frac{\mu}{Pr} \frac{\partial T}{\partial x_j} \quad (5)$$

where  $S_{ij}$  is the strain-rate tensor,  $\mu$  the dynamic viscosity, respectively given by  $S_{ij} = \frac{1}{2} \left( \frac{\partial u_j}{\partial x_i} + \frac{\partial u_i}{\partial x_j} \right)$ ,  $\mu = T^n$  where  $n = 0.75$  is the viscosity exponent and  $Pr$  is the Prandtl number.

The governing equations (2), (3), (4) are discretized on a Cartesian domain and solved with the high-order structured code *Hybrid*, developed by Johan Larrson [16, 15] originally for numerical investigation of the fundamental canonical shock-turbulence interaction problem. The code has been scaled up to 1.97 million cores in recent remarkable computational efforts by Bermejo-Moreno [2]. A solution-adaptive strategy is employed to blend high-order central polynomial and WENO schemes in presence of strong flow gradient [1, 20]. A fourth order discretization both in space and time has been adopted in the present work.

The computational domain considered for the turbulent simulations in this study is  $L_x \times L_y \times L_z = 8 \times 2 \times 4$  which is discretized with a number of control volumes  $N_x \times N_y \times N_z = 256 \times 128 \times 192$  resulting in a quasi-DNS resolution of  $\Delta x^+ \sim 12.27 - 13.22$ ,  $\Delta z^+ \sim 8.17 - 8.81$ ,  $\Delta y^+_{\min} = 0.45 - 0.47$ , over the range of bulk Mach numbers investigated. The superscript  $+$  indicates classic wall-units,  $\delta_V = u_\tau \rho_w / \mu_w$ , where  $u_\tau = \sqrt{\tau_w / \rho_w}$  is the friction velocity and  $\rho_w$  and  $\mu_w$  are the density and dynamic viscosity evaluated at the wall and the wall-shear stress is  $\tau_w = \mu_w \overline{\partial \bar{u} / \partial y}|_w$  where  $\overline{(\ )}$  indicates Reynolds averaging.

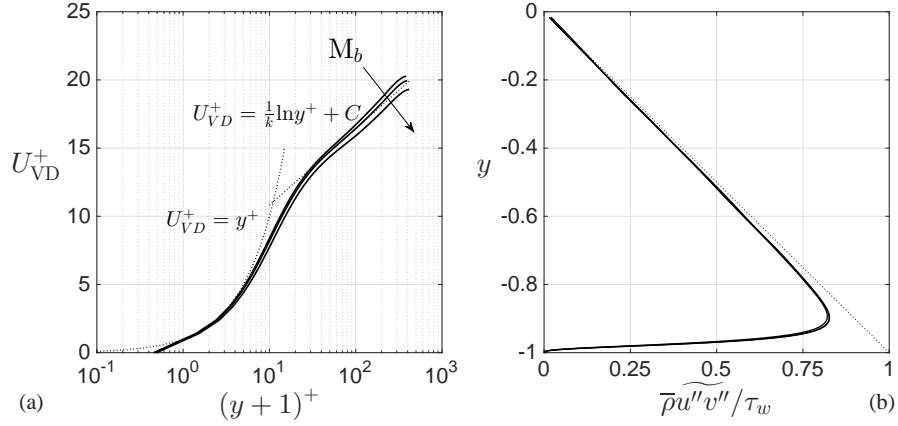


Fig. 1: Profiles of turbulent mean velocity following Van Driest transform with reference law of the wall and log-law  $k = 0.41$  and  $C = 5.2$  (···) (a) and Reynolds stresses along with linear total shear stress (b)

Mean velocity profiles in figure (1 a) are plotted using Van Driest transform following

$$U_{VD}^+ = \int_0^{U^+} \left( \frac{\rho}{\rho_w} \right)^{1/2} dU^+ = \frac{1}{\kappa} \ln y^+ + C \quad (6)$$

In this set of simulations, friction Reynolds number  $\text{Re}_\tau = u_\tau/\delta/\nu$  varies from 385.6 to 417.4. Reynolds stress profiles in figure (1b) are plotted based on the semi-local scaling proposed by Huang et al. [12]. In this procedure the semi-local friction velocity is  $u_\tau^* = \tau_w/\bar{\rho}$  is known to be the reference velocity, with  $\bar{u}$  being the Reynolds-averaged streamwise velocity. The semi-local wall-normal coordinate is defined as  $y^* = y/\delta_v^*$  where the semi-local viscous unit is  $\delta_v^* = \bar{\mu}/(\bar{\rho}u_\tau^*)$ . This figure suggests that near wall turbulence behavior is kept constant by varying the Mach number.

Resolution of the numerical results based on semi-local scaling is  $\Delta x^* \sim 11.12 - 12.74$ ,  $\Delta z^* \sim 7.14 - 8.50$ ,  $\Delta y_{\min}^* = 0.45 - 0.47$ . Collapse of both mean velocity and Reynolds Stress profiles is obtained, showing that the state of near-wall turbulence has been successfully kept constant while varying the bulk Mach number.

The laminar flow results have been generated with the same code with  $N_y = 192$  control volumes in the wall-normal direction, for the same combination of  $Re_b$  and  $M_b$  as for the turbulent simulations.

## 2.2 Linearized Equations

Decomposing a generic instantaneous quantity,  $a(x, y, z)$  into a base state,  $\mathcal{A}(y)$ , and a two-dimensional fluctuation,  $a'(x, y, t)$ , assuming ideal gas behaviour yields the following equations for conservation of mass, streamwise and wall-normal momentum, and energy [19]:

$$\begin{aligned} \frac{\gamma}{\mathcal{T}} \frac{\partial p'}{\partial t} - \frac{1}{\mathcal{T}^2} \frac{\partial T'}{\partial t} + \frac{1}{\mathcal{T}} \frac{\partial u'}{\partial x} + \mathcal{U} \left( \frac{\gamma}{\mathcal{T}} \frac{\partial p'}{\partial x} - \frac{1}{\mathcal{T}^2} \frac{\partial T'}{\partial x} \right) + \frac{1}{\mathcal{T}} \frac{\partial v'}{\partial y} - \frac{1}{\mathcal{T}^2} \frac{\partial \mathcal{T}}{\partial y} v' &= 0 \quad (7) \\ \left( \frac{\partial u'}{\partial t} + \mathcal{U} \frac{\partial u'}{\partial x} + v' \frac{\partial \mathcal{U}}{\partial y} \right) \frac{1}{\mathcal{T}} &= - \frac{\partial p'}{\partial x} + \frac{\mu}{\text{Re}_a} \left[ l_2 \frac{\partial^2 u'}{\partial x^2} + l_1 \left( \frac{\partial^2 v'}{\partial x \partial y} \right) + \frac{\partial^2 u'}{\partial y^2} + \right. \\ \left. \frac{1}{\mu} \frac{d\mu}{d\mathcal{T}} \frac{dT}{dy} \left( \frac{\partial u'}{\partial y} + \frac{\partial v'}{\partial x} \right) + \frac{1}{\mu} \frac{\partial \mu}{\partial \mathcal{T}} \left( \frac{\partial^2 \mathcal{U}}{\partial y^2} T' + \frac{\partial \mathcal{U}}{\partial y} \frac{\partial T'}{\partial y} \right) + \frac{1}{\mu} \frac{\partial^2 \mu}{\partial \mathcal{T}^2} \frac{\partial \mathcal{T}}{\partial y} \frac{\partial \mathcal{U}}{\partial y} T' \right] & \quad (8) \end{aligned}$$

$$\begin{aligned} \left( \frac{\partial v'}{\partial t} + \mathcal{U} \frac{\partial v'}{\partial x} \right) \frac{1}{\mathcal{T}} &= - \frac{\partial p'}{\partial y} + \frac{\mu}{\text{Re}_a} \left[ \frac{\partial^2 v'}{\partial x^2} + l_1 \left( \frac{\partial^2 u'}{\partial x \partial y} \right) + l_2 \frac{\partial^2 v'}{\partial y^2} + \dots \right. \\ \left. + \frac{1}{\mu} \frac{\partial \mu}{\partial \mathcal{T}} \left( \frac{\partial T'}{\partial x} \frac{\partial \mathcal{U}}{\partial y} \right) + \frac{1}{\mu} \frac{\partial \mu}{\partial \mathcal{T}} \frac{\partial \mathcal{T}}{\partial y} \left\{ l_0 \left( \frac{\partial u'}{\partial x} \right) + l_2 \frac{\partial v'}{\partial y} \right\} \right] & \quad (9) \end{aligned}$$

$$\begin{aligned}
\left(\frac{\partial T'}{\partial t} + \mathcal{U}\frac{\partial T'}{\partial x} + v'\frac{\partial T'}{\partial y}\right)\frac{1}{\mathcal{T}} &= (\gamma-1)\left[\frac{\partial p'}{\partial t} + \mathcal{U}\frac{\partial p'}{\partial x}\right] + \dots \\
+ \frac{\mu}{\text{Re}_a \text{Pr}} \left[ \frac{\partial^2 T'}{\partial x^2} + \frac{\partial^2 T'}{\partial y^2} + \frac{2}{k} \frac{\partial k}{\partial \mathcal{T}} \frac{\partial \mathcal{T}}{\partial y} \frac{\partial T'}{\partial y} + \left( \frac{1}{k} \frac{\partial k}{\partial \mathcal{T}} \frac{\partial^2 \mathcal{T}}{\partial y^2} + \frac{1}{k} \frac{\partial^2 k}{\partial \mathcal{T}^2} \left(\frac{\partial \mathcal{T}}{\partial y}\right)^2 \right) T' \right] &+ \\
\dots + \frac{(\gamma-1)\mu}{\text{Re}_a} \left[ +2 \frac{\partial \mathcal{U}}{\partial y} \left( \frac{\partial u'}{\partial y} + \frac{\partial v'}{\partial x} \right) + \frac{1}{\mu} \frac{\partial \mu}{\partial \mathcal{T}} \left( \frac{\partial \mathcal{U}}{\partial y} \right)^2 \right] &
\end{aligned} \tag{10}$$

where  $l_j = j + \frac{\lambda}{\mu}$  and  $\lambda = -\frac{2}{3}\mu$ ,  $\mu = \mathcal{T}^n$ ,  $k = Cp\mu/Pr$  where  $\mathcal{T}$  is the base temperature and  $\mathcal{U}$  denotes the base streamwise velocity. Eddy viscosity effects on the fluctuations have been ignored in the scope of this analysis. Assuming harmonic fluctuations

$$a'(x, y, t) = \hat{a}(y)e^{i(\alpha x - \omega t)} = \hat{a}(y)e^{i\alpha(x - ct)} \tag{11}$$

where  $\alpha$  is the wavenumber in the streamwise direction and  $\omega = \alpha c$  and  $c = c_r + ic_i$  are the complex frequency and complex wave (or phase) speed. Applying a Gauss-Lobatto-Chebyshev discretization along the wall-normal direction yields the generalized eigenvalue problem

$$\mathbf{A} \cdot \boldsymbol{\Psi} = \omega \mathbf{B} \cdot \boldsymbol{\Psi} \tag{12}$$

with  $\boldsymbol{\Psi} = \{\hat{\mathbf{u}}; \hat{\mathbf{v}}; \hat{\mathbf{p}}; \hat{\mathbf{T}}\}$  where the generic column vector  $\hat{\mathbf{a}}$  collects of discretized complex amplitudes of the generic fluctuating variable,  $a'$ . Four conditions at each boundary are needed to close the system (12) and they are: no slip conditions for the streamwise velocity component,  $\hat{u} = 0$ ; isothermal conditions for temperature fluctuations,  $\hat{T} = 0$ ; impedance boundary conditions  $\hat{p} = \mp R \hat{v}$  for  $y \pm 1$  (upper and lower wall, respectively); Non-homogeneous Neumann conditions for wall-normal derivative of pressure derived by extending (9) at the boundary.

Including the aforementioned boundary conditions in the system (12), yields a singular  $\mathbf{B}$  matrix. Eigenvalues obtained by directly solving the general eigenvalue problem in this form yields eigenfunctions contaminated by numerical noise, despite eigenvalues still being accurate. This problem has been solved by reconditioning the system by recasting (12) into

$$\omega^{-1} \boldsymbol{\Psi} = \mathbf{A}^{-1} \mathbf{B} \cdot \boldsymbol{\Psi} \tag{13}$$

and solving the eigenvalue problem directly for the matrix  $\mathbf{C} = \mathbf{A}^{-1} \mathbf{B}$  [7]. While this technique considerably improves the quality of the eigenfunctions, results for high wave-numbers ( $\alpha > 2$ ) still exhibit some minor numerical issues such as slight top-down anti-symmetry. Use of low-order schemes and staggered grid variable arrangement may solve these problems, and it will be explored in future studies.

Following Friedrich and Bertolotti [8], the base flow is chosen to match Reynolds-averaged quantities, ( $\mathcal{U} = \bar{u}$  and  $\mathcal{T} = \bar{T}$ ) indicated with  $\bar{(\ )}$ . The mean pressure in a boundary layer can be assumed constant  $\mathcal{P} = 1/\gamma$  so the mean density is derived by

applying the equation of state. However, to match the turbulent statistics carried out in Coleman et. al [4]  $\mathcal{P}$  is set to 0.1883. The actual value of  $\mathcal{P}$  is not reported in [8].

### 3 Comparison Against Previous LSA

#### 3.1 Compressible Couette Flow

Validation is first carried out against LSA results for compressible Couette flow by Hu and Zhong [10, 11], where iso-thermal conditions,  $T_\infty = 1$ , and the tangential velocity,  $U_\infty$  are imposed at the top wall, and no-slip and adiabatic conditions at the bottom wall. Reynolds number and Mach number based on the topwall velocity are  $Re_\infty$  and  $M_\infty$ . All quantities are normalized with speed of sound based on top wall temperature, the bulk density and the total wall-to-wall distance. For the present validation, the dynamic viscosity have been changed with respect to section 2.2 and are set to

$$\mu = \mathcal{T}^{1.5} \frac{1+C}{\mathcal{T}+C}, \quad C = 0.5 \quad (14)$$

and Prandtl number  $Pr = 0.72$ , to match Hu and Zhong [10, 11]. Excellent agreement is found as shown by the eigenvalue spectra and eigenfunctions and a grid convergence study of the eigenvalues (table 1) which includes results from more recent LSA work on Couette flow by Weder [28].

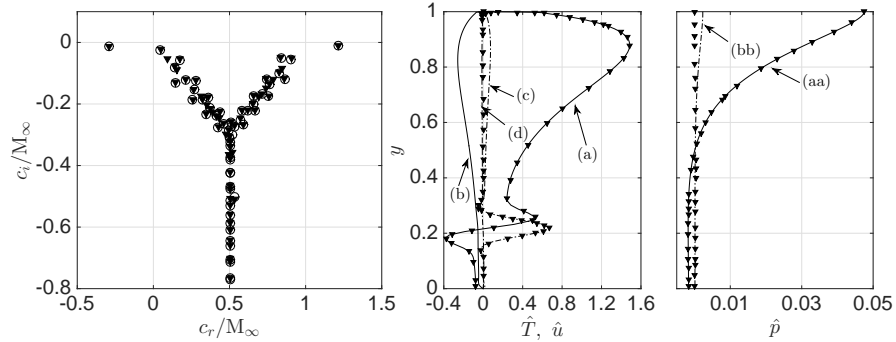


Fig. 2: Comparison of complex phase velocity spectrum for compressible Couette flow at  $M_\infty = 2$ ,  $Re_\infty = 2 \times 10^5$ ,  $\alpha = 1$  using  $N=100$  grid points ( $\circ$ ) with results from Hu and Zhong [11] ( $\blacktriangledown$ ). Real part (—) and imaginary part (---) of velocity,  $\hat{u}$ , temperature,  $\hat{T}$ , and pressure,  $\hat{p}$ , eigenfunctions of the most unstable mode at  $M_\infty = 5$ ,  $Re_\infty = 5 \times 10^5$ ,  $\alpha = 3$  with (a):  $Re\{\hat{T}\}$ , (b):  $Re\{\hat{u}\}$ , (c):  $Im\{\hat{T}\}$ , (d):  $Im\{\hat{u}\}$ , (aa):  $Re\{\hat{p}\}$ , (bb):  $Im\{\hat{p}\}$ .

Table 1: Comparison of complex wave speed,  $c$ , of the most unstable mode for compressible Couette flow with previously published results for various  $Re_\infty$ ,  $M_\infty$  and  $\alpha$ . Grid convergence study shown for  $N=100$ ,  $N=200$  and  $N=300$ , respectively, top, middle and bottom rows for each case. Deviating digits from Hu and Zhong data [10] are underlined. Values of  $c$  have been normalized with the top-wall Mach number,  $M_\infty$ , to match published values.

Hu and Zhong [10]		Weder [28]		Current Study	
$c_r/M_\infty$	$c_i/M_\infty$	$c_r/M_\infty$	$c_i/M_\infty$	$c_r/M_\infty$	$c_i/M_\infty$
Re <sub>∞</sub> = 5 × 10 <sup>6</sup> , M <sub>∞</sub> = 5, α = 2.1, Mode I					
+0.972869314676	-0.003456356315	+0.972869 <u>178324</u>	-0.003456358661	+0.972869 <u>280518</u>	-0.003456323886
+0.972869272448	-0.003456466520	+0.972869 <u>198693</u>	-0.003456318849	+0.97286927244 <u>5</u>	-0.00345646674 <u>3</u>
+0.972869272450	-0.003456466522	+0.972869 <u>201921</u>	-0.003456324875	+0.972869272 <u>355</u>	-0.003456466505
Re <sub>∞</sub> = 5 × 10 <sup>6</sup> , M <sub>∞</sub> = 5, α = 2.1, Mode 0					
+0.040730741952	+0.000876050503	+0.0407 <u>26205831</u>	+0.000884153855	+0.040730596292	+0.000874754264
+0.040722854287	+0.000885530891	+0.04072285 <u>3306</u>	+0.000885531375	+0.040722854 <u>373</u>	+0.000885530566
+0.040722853034	+0.000885531421	+0.04072285 <u>3219</u>	+0.000885531398	+0.04072285303 <u>2</u>	+0.000885531421
Re <sub>∞</sub> = 2 × 10 <sup>5</sup> , M <sub>∞</sub> = 2, α = 0.1, Mode I					
+1.213965119859	-0.011585118523	+1.21396511985 <u>1</u>	-0.011585118549	+1.21396511985 <u>1</u>	-0.011585118547
+1.213965119817	-0.011585118448	+1.21396511985 <u>2</u>	-0.011585118548	+1.21396511985 <u>2</u>	-0.011585118547
+1.213965119854	-0.011585118558	+1.21396511985 <u>1</u>	-0.011585118548	+1.21396511985 <u>2</u>	-0.011585118547
Re <sub>∞</sub> = 2 × 10 <sup>5</sup> , M <sub>∞</sub> = 2, α = 0.1, Mode 0					
-0.291572925106	-0.013821128462	-0.2915729251 <u>10</u>	-0.013821128465	-0.291572925109	-0.013821128464
-0.291572925140	-0.013821128536	-0.2915729251 <u>16</u>	-0.013821128473	-0.291572925109	-0.013821128464
-0.291572925108	-0.013821128457	-0.2915729251 <u>12</u>	-0.013821128467	-0.291572925109	-0.013821128464

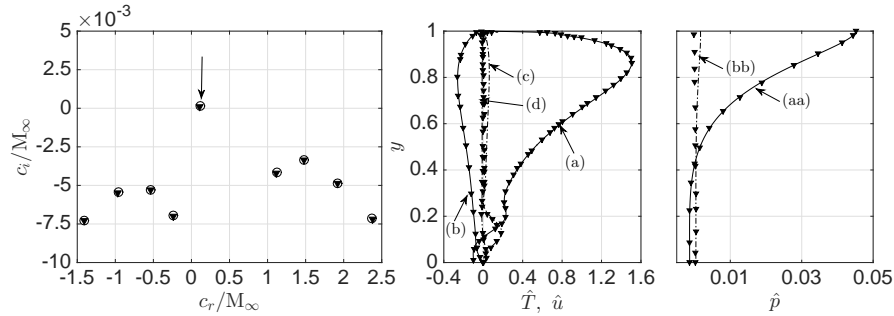


Fig. 3: Comparison of complex phase velocity spectrum for laminar compressible Couette flow at  $M_\infty = 5$ ,  $Re_\infty = 1.10^5$  and  $\alpha = 2.5$  using  $N=100$  grid points ( $\blacktriangledown$ ) against Hu and Zhong [10]. Real part (—) and imaginary part (---) of velocity,  $\hat{u}$ , temperature,  $\hat{T}$ , and pressure,  $\hat{p}$ , eigenfunctions of the most unstable mode (indicated with downward arrow) with (a):  $Re\{\hat{T}\}$ , (b):  $Re\{\hat{u}\}$ , (c):  $Im\{\hat{T}\}$ , (d):  $Im\{\hat{u}\}$ , (aa):  $Re\{\hat{p}\}$ , (bb):  $Im\{\hat{p}\}$ .



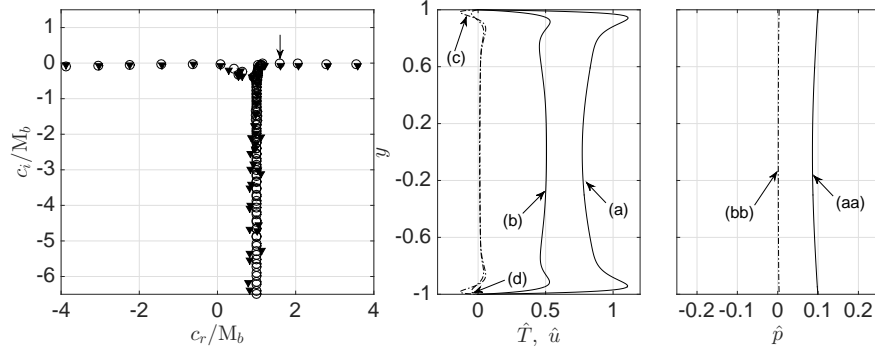


Fig. 4: Complex phase velocity spectrum for compressible channel flow at  $M_b = 0.5$ ,  $Re_c = 4880$  and  $\alpha = 1$  using  $N = 165$  grid points ( $\circ$ ) compared with data from Friedrich and Bertolotti [8] ( $\blacktriangledown$ ). Real part (—) and imaginary part (— · —) of eigenfunctions of the most unstable mode indicated with a downward arrow. (a):  $Re\{\hat{T}\}$ , (b):  $Re\{\hat{u}\}$ , (c):  $Im\{\hat{T}\}$ , (d):  $Im\{\hat{u}\}$ , (aa):  $Re\{\hat{p}\}$ , (bb):  $Im\{\hat{p}\}$

### 3.2 Compressible Channel Flow

Friedrich and Bertolotti [8] performed a stability analysis of compressible turbulent channel flow at  $Re_c=4880$  based on the centerline velocity,  $M_b = 3$ ,  $\alpha = 1$  using Parabolized Stability Equation (PSE) with a multi-domain spectral discretization method. The base flow was taken from the Reynolds-averaged velocity and temperature profiles in Coleman et al. [4]. The eigenvalue spectrum is compared in figure 4 where eigenfunctions of the most unstable mode (not originally plotted in their paper) are also included. Despite the fundamental difference between our (classic) LSA approach and their PSE, the agreement is still acceptable. Values for viscosity and value of Prandtl number are the same as the ones used in section 3.1. Friedrich and Bertolotti [8] did not explicitly mention what law for viscosity has been used, therefore the results in figure 5 have been reproduced assuming  $\mu = \mathcal{T}^n$ , consistent with the simulations by Coleman et al. [4].

## 4 Effects of Porous Walls

Laminar and Reynolds-averaged turbulent mean profiles from impermeable isothermal wall compressible channel flow calculations at  $Re_b = 6900$  and  $M_b = 0.2, 0.5, 0.85$  (figure 5) are used as the base flow for the following LSA investigating the effect of porous walls on the disturbance. Since turbulent eddy viscosity is neglected, the nature of the instability between laminar and turbulent cases only differs due to the shape of base flow profiles. In particular, the spatial distribution of the wall-normal gradient of the mean streamwise velocity plays a fundamental role in shap-

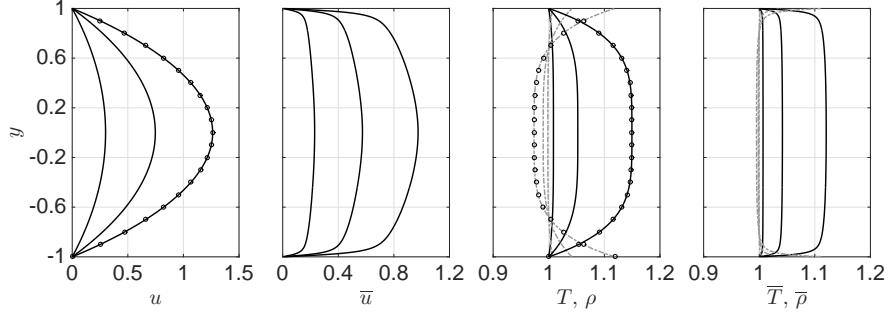


Fig. 5: Profiles of laminar velocity,  $u(y)$ , temperature,  $T(y)$ , and density  $\rho(y)$  and Reynolds-averaged turbulent velocity,  $\bar{u}(y)$ , temperature,  $\bar{T}(y)$ , and density  $\bar{\rho}(y)$  at  $Re_b = 6900$  and  $M_b = 0.2, 0.5$ , and  $0.85$ . For validation purposes, laminar values are calculated at  $Re_b = 6900$  and  $M_b = 0.85$  assuming periodicity in streamwise and spanwise directions using second order finite difference and showed by circles

ing the unstable modes triggered by the wall permeability and determining the location of the energy production regions.

#### 4.1 Eigenvalues trajectory

A parametric study has been performed by varying the impedance resistance,  $R$ , from  $R \rightarrow \infty$  (zero permeability) to  $R = 0.01$  (high permeability) in both laminar and turbulent cases, two modes, Mode 0 and Mode 1, initially localized on the left branch of the impermeable wall eigenvalue spectrum are made unstable ( $c_i > 0$ ) for a sufficiently low value of resistance  $R < R_{cr}$  (figure 6). In all cases, monotonically with increasing the permeability, the phase speed of the unstable modes increases, exceeding the bulk flow velocity eventually.

In the laminar case, for  $\alpha = 1$ , the two modes originates from different regions of the eigenvalue spectrum. Mode I at  $R \rightarrow \infty$  exhibits a very slow decay rate, requiring low values of permeability (high value of resistance  $R_{cr} = 1$ ) to become unstable. For near-impermeable conditions, Mode 0 is instead located close to the junction of Y-shape spectrum (phase velocity approximately equal to the bulk velocity) and becomes unstable at a much lower values of resistance  $R_{cr} \sim 0.05$ . As discussed later, their difference in shape is not related to their different location in the eigenvalue spectrum or critical values. As  $\alpha$  increases (not shown), the two starting points, and the corresponding trajectories, become closer such that at  $\alpha = 2$  they start from two adjacent nodes at the middle of the left branch of Y-spectrum. Decreasing  $\alpha$  yields the opposite effect with trajectories originating from opposite edge Y spectrum for  $\alpha = 0.1$ .

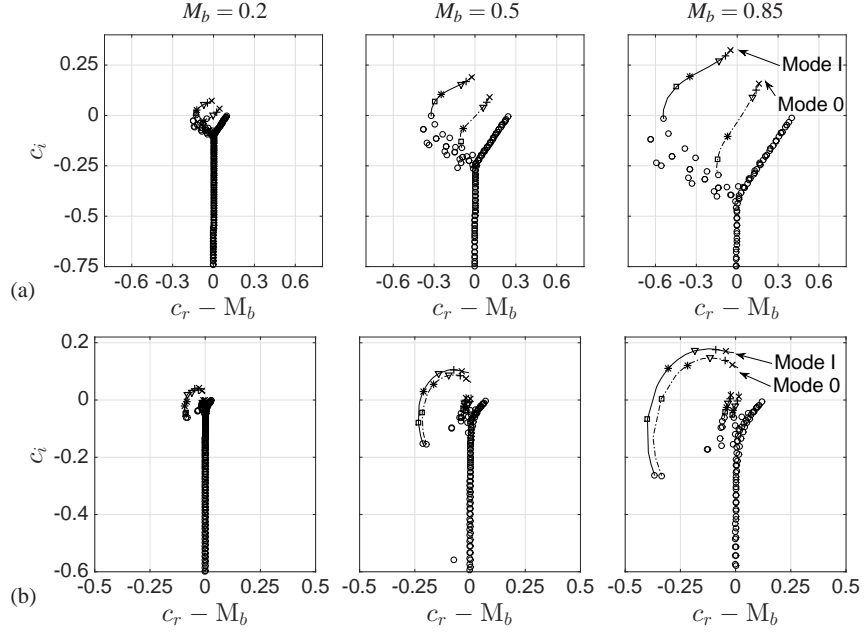


Fig. 6: Trajectory of Mode 0 and Mode 1 for  $k=1$  in the complex phase velocity spectrum of compressible channel flow with impedance boundary conditions (1) using laminar (a) and turbulent (b) base flow at  $Re_b = 6900$ ,  $M_b = 0.85$  traced by varying the impedance resistance in the range  $R = 10 - 0.01$  for  $N = 200$  grid points. In increasing order of permeability,  $R \rightarrow \infty$  (zero permeability):  $(\circ)$ ,  $R = 1$ :  $\square$ ,  $R = 0.5$ :  $*$ ,  $R = 0.1$ :  $\nabla$ ,  $R = 0.05$ :  $+$ ,  $R = 0.01$ :  $\times$ .

The baseline impermeable-wall spectrum for  $\alpha = 1$  does not exhibit a clear Y-shape for the turbulent case. The trajectories of the modes follow very similar paths for the range of  $\alpha = 0.1 - 2$  tested and share very similar values of critical impedance resistance (or wall permeability), suggesting their coexistence. This behavior is due to the *flatness* of the velocity profile, which is accentuated in the case of fully developed turbulence over tuned wall impedance, as observed by Scalo et al. [22].

The growth rate of the unstable mode, in case of laminar base flow, increases monotonically for decreasing  $R$  in the range investigated. However, when using turbulent base flow, the growth rate saturates and then decreases for the same range of  $R$ . For the turbulent case only, two new unstable modes (with a similar pairing behavior as Mode 0 and Mode I) originate from the central part of the spectrum. They are not present in the laminar base flow case and travel at roughly the bulk velocity,  $c_r - M_b \sim 0$ , become unstable, for very low values of resistance  $R_{cr} \sim 0.05$ . A detailed study of them is deferred to future work.

The transition from subcritical to supercritical permeability does not qualitatively alter the structure of Mode 0 and Mode 1; both modes retain a very pronounced acoustic-like structure in the core of the channel (figure 7), even in the impermeable wall limit. For the range of  $\alpha$  and Mach numbers investigated, Mode 0 always manifests as a bulk pressure mode, causing symmetric expulsion and suction of mass from the porous walls, whereas Mode 1 resembles a standing-wave, with a pressure node at the channel's centerline. The only exception is Mode 0, with laminar base flow profiles at subcritical permeabilities which does not exhibit an appreciable structural coherence.

For increasing wavenumber, a thinning of the boundary layer of the perturbation is observed, extending the inviscid core region, where acoustic-like dynamics are observed, suggesting a scaling following the Stokes boundary layer thickness  $\delta_s = \sqrt{2\nu/\omega_r} = \sqrt{2\nu/(\alpha c_r)}$ . The relative intensity of the wall-normal transpiration with respect to the centerline value of  $|\hat{v}|$  increases with  $\alpha$  for both modes (figure 7a).

As permeability increases, the shape of Mode I deviates more from a typical standing-wave (with a pressure node on channel's centerline) with two new pressure modes appearing in the near wall region. It also causes an increase the in relative intensity of the wall-normal transpiration with respect to  $\hat{v}_c$  in Mode 0 (see figure 7b). Varying bulk Mach number, in the range considered herein, does not significantly alter the structure of both modes (figure 7 c).

## 4.2 Reynolds stresses

Results from the present LSA can be used to infer the shape of the Reynolds stresses resulting from the application of porous walls which have been calculated as

$$\tilde{R}_{12} = \frac{Re\{\hat{u}\hat{v}^*\}}{\int_{-1}^0 Re\{\hat{u}\hat{v}^*\} dy} \quad (15)$$

In the case of turbulent mean flow profiles, both modes generate an anti-symmetric Reynolds stress distribution concentrated in base flow's viscous sublayer (figure 1b) with negligible effects in the turbulent core  $-0.9 < y < 0.9$ .

Normalized Reynolds stress for Mode 0 using laminar base flow do not change considerably when permeability varies. However, these profiles are incoherent for subcritical permeabilities, as also pointed out in section 4.1. Results for Mode I show that Reynolds stress peak tends to approach the wall for increasing the permeability (decreasing  $R$  value).

Employing turbulent base flow, Reynolds stress shape for both modes exhibits similar features with some minor changes. Decreasing  $R$  value can lead to a profile whose maximum point gets closer to the wall. Value of normalized Reynolds stress decays much faster than the case employing laminar base flow so that this quantity becomes very small at  $y \sim 0.8$  for all  $R$  values. In the other end,  $\tilde{R}_{12}$  has a significant value until the half channel when incorporating laminar base flow.

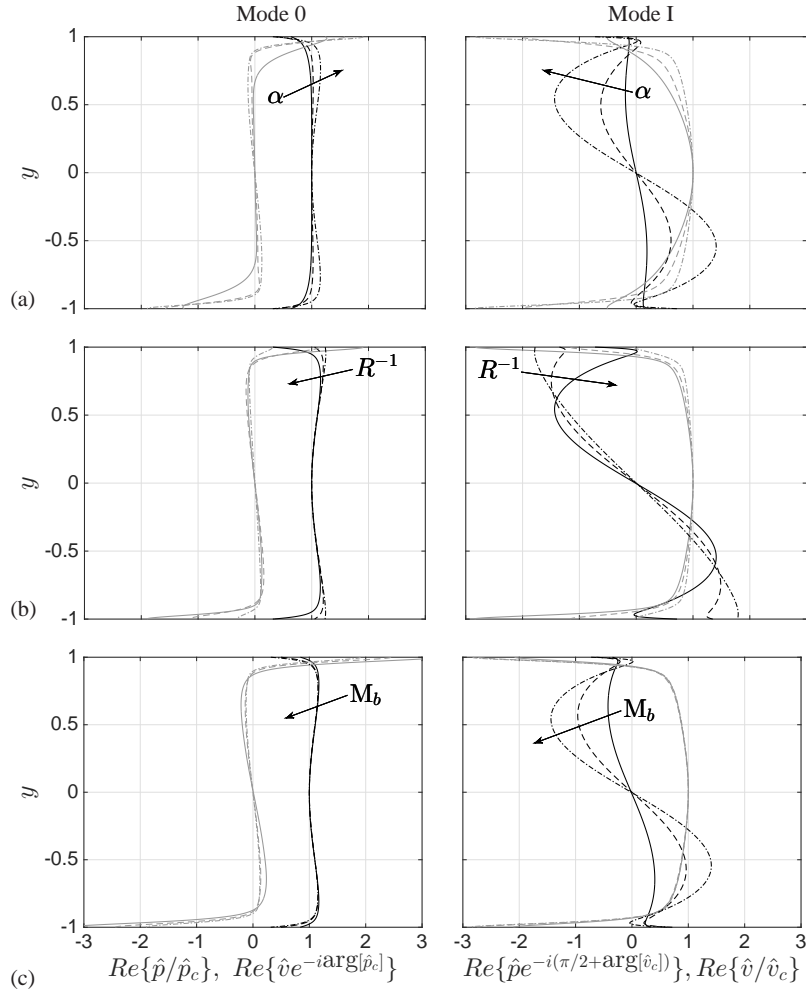


Fig. 7: Comparison between Mode 0 (left) and Mode 1 (right) showing pressure,  $\hat{p}$ , (black) and wall-normal velocity,  $\hat{v}$  (grey) eigenfunctions with base flow taken from turbulent mean profiles at  $Re_b = 6900$ . Resistance  $R = 0.01$  and  $M_b = 0.85$ , for wavenumbers  $\alpha = 0.1$  (—),  $\alpha = 0.5$  (---), and  $\alpha = 1.0$  (-·-) (a); Wavenumber  $\alpha = 1$  and  $M_b = 0.85$ , for resistances  $R = 1.0$  (-·-),  $R = 0.1$  (---), and  $R = 0.01$  (—) (b). Wavenumber  $\alpha = 1$  and  $M_b = 0.85$ , for bulk Mach numbers  $M_b = 0.2$  (—),  $M_b = 0.5$  (---), and  $M_b = 0.85$  (-·-) (c). In all Mode 0 plots, all pressure eigenfunctions have been normalized with their value at the centerline,  $\hat{p}_c$ ; the resulting phase shift has been applied to the eigenfunctions of wall-normal velocity. In all Mode 1 plots, the vertical velocity eigenfunctions have been normalized with their value at the centerline,  $\hat{v}_c$ , the pressure eigenfunctions' phase shifted accordingly and then further changed by  $90^\circ$  to show the standing-wave-like structure in the channel core.

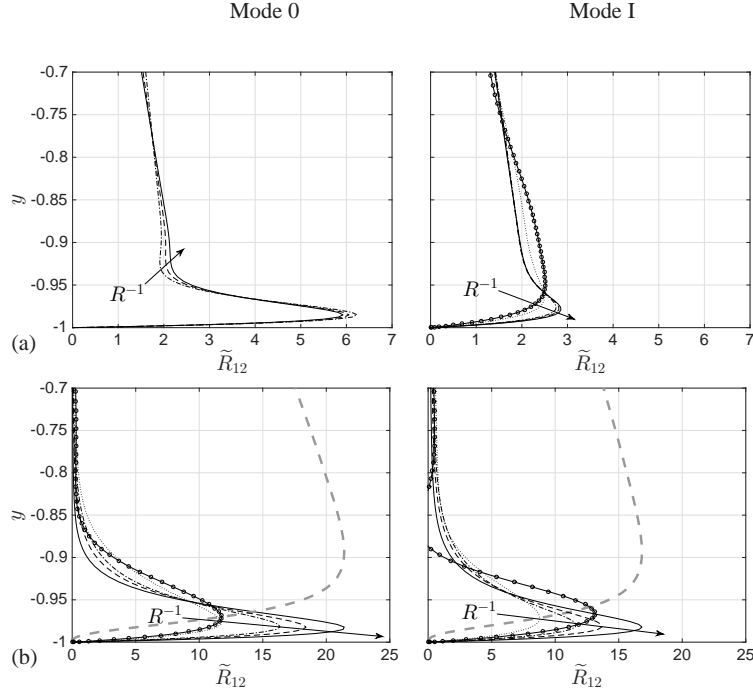


Fig. 8: Near-wall profiles of normalized Reynolds shear stresses  $\tilde{R}_{12}$  (15) for Mode 0 (left) and Mode 1 (right) predicted by LSA for  $N = 200$  grid points, for different values of resistance,  $R$ , and  $\alpha = 1$  with base flow taken from laminar (a) and turbulent (b) channel flow calculations at  $Re_b = 6900$ ,  $M_b = 0.85$ . Arrows indicate increasing values of permeability (decreasing value of resistance) with  $R = 1$  ( $\circ$ ),  $R = 0.5$  ( $\cdot\cdot$ ),  $R = 0.1$  ( $-\cdot-\cdot-$ ),  $R = 0.05$  ( $- - -$ ),  $R = 0.01$  ( $—$ ). Results for  $R=1$  and  $R=0.5$  are omitted for Mode 0 with a laminar base profile, since corresponding eigenmodes do not exhibit a coherent structure. Turbulent Reynolds stresses from figure 1 are reported here (in arbitrary units) with thick dashed grey lines.

It should be noted that changing the porosity results in a considerable variation in the growth rate of the disturbance which is expected to yield (quantitatively) more intense Reynolds stress for lower  $R$ .

Caution should be used when comparing the absolute value of Reynolds stresses in case of employing laminar base flow with turbulent base flow without a calibration study. Probst and co-workers [21] employed similar data for flow over a flat plate along with some preliminary assumptions to build a transition model based on the linear stability analysis. They showed that a scaling factor can be found which delivers reliable values for Reynolds stress from these shapes which for a boundary layer it can be a function of edge velocity and  $\hat{u}_{max}^2$ .

This mode is of interest since it shows analogies with the Kelvin-Helmholtz instability observed by Scalò et al [22], who have revealed the presence of a hydro-

dynamic instability due to acoustic resonance generated by the interaction of a compressible boundary layer with a damped Helmholtz resonators at the wall. This resulted in very coherent, quasi-two-dimensional structures which revealed properties typical of Kelvin-Helmholtz instability. The excess in Reynolds stresses detected was uniquely due to such two-dimensional instability and was observed to occur in the viscous sublayer.

## 5 Discussion and Future Work

In the present paper, Linear Stability Analysis (LSA) is employed to predict the effects of permeability on a laminar and turbulent compressible channel flow up to transonic bulk Mach numbers. Two dimensional, streamwise periodic disturbances are considered and porous walls are modeled by linear acoustic impedance boundary conditions with zero reactance, with resistance,  $R$  (inversely proportional to the wall-permeability) varying in the range,  $R = 1 - 0.01$ .

To investigate the effects of the base flow on the stability properties of the perturbation field, both laminar and turbulent base states are considered. They are obtained from numerical simulations of compressible channel flow with isothermal, no-penetration walls (hard walls) carried out for bulk Mach numbers  $M_b = [0.2, 0.5, 0.85]$ , all at a constant bulk Reynolds Number  $Re_b = 6900$ , under both laminar and turbulent flow conditions.

Increasing the permeability,  $R^{-1}$  destabilizes the flow by triggering two modes; one characterized by bulk (quasi-uniform) pressure oscillations in the core, with gradients of fluctuating quantities concentrated in the near wall viscous region (Mode 0); one resembling an acoustic standing wave resonating in the channel's core, with similar near-wall behavior (Mode I). Symmetric eigenfunctions for  $u'$ ,  $T'$ , and  $p'$  are observed for 'Mode 0', while  $v'$  is anti-symmetric. The latter is associated with an anti-symmetric, time periodic, expulsion and suction of mass from the boundaries driven by the bulk pressure fluctuations in the core. On the other hand, Mode 1 exhibits anti-symmetric  $u'$ ,  $T'$ , and  $p'$  instantaneous profiles, while  $v'$  retains top-down symmetry. Increasing the wall permeability causes the perturbation-induced Reynolds shear-stress distribution to shift closer to the porous walls for both laminar and turbulent base flows.

For very high values of permeability ( $R < 0.01$ ) – approaching unrealistic values, based on measurements the acoustic response of perforated panels by [23] – and only in the case of a turbulent base flow, a saturation of the growth rate is observed.

Although the current analysis is limited to purely real acoustic impedances (i.e. classic Darcy-like formulation for porous walls), the results obtained qualitatively confirm the structure of the hydro-acoustic instability observed by Scalo et al., PoF, 2015 [22]. In their case, large spanwise-coherent Kelvin-Helmholtz rollers (with strong induced Reynolds shear stresses) are found to be confined near the wall, while the outer layer remained unaffected. This result is in qualitative agreement with the perturbation-induced Reynolds shear stress distribution predicted by the

current analysis and in contrast with the findings by Jiménez et al. [14], valid for the incompressible limit. A more accurate comparison between our LSA and the results by Scalo et al., PoF, 2015 [22] will be obtained in future studies, which will incorporate a broadband reactance (the impedance's imaginary part) in the eigenvalue problem.

Eigenvalue tracking shows that the modes made unstable by permeability, preserve their structure as stable modes in the hard wall case. Only in the laminar case, Mode 1 is at the verge of instability for zero permeability. As the wavenumber  $\alpha$  is increased, trajectory of the unstable modes become close to each other, and near-wall gradients of fluctuating quantities intensify.

Future work will focus on Direct Numerical Simulation of channel flow with general impedance boundary conditions and new companion LSA efforts with improved numerics and physical modeling of the boundary conditions. Investigations will be also carried out considering boundary layers over flat plates, since confinement effects might also play a role in the hydro-acoustic instability observed by Scalo et al., PoF, 2015.

## 6 From Small Data to Big Data (and viceversa)

This work has been centered around use of *small* data, in the form of a classic Linear Stability Analysis, in order to acquire a general understanding of the response that it is expected from compressible channel flow turbulence under the effects of porous walls. This problem can only be truly explored in detail with large-scale, high-fidelity simulations, that is, *big* data. Simplified, low-order models are, however, essential in guiding the design and interpretation of companion large-scale numerical simulations, since they allow us to focus on the core of the phenomenon under investigation, providing a rough but robust understanding of the physical problem at a considerably reduced cost. Moreover, this approach allows us to perform a true parametric study, spanning, for example, several orders of magnitude of variation of a key parameter in the problem, such as, in this case, the wall permeability. High-fidelity simulations can be used to populate a few key regions in the parameter space to investigate, with limited modeling errors. A synergistic interaction between small data and big data should be sought, rather than a "blind big data"- or a "blind small data"- only approach, since both may suffer from severe limitations. The development, analysis and adoption of the two approaches should therefore go hand in hand. With the advances in computational power, the definition of small and big data is changing rapidly. For example, turbulence simulations performed on a computational grid of  $N^3 = 1024^3$  points, can today (2015) be considered *average-size* data. In spite of paradigm shifts dictated by the ever growing increase in available computational power, we believe that the importance of low-order models (used here as an example of small data) will never (and should never) cease to retain a prominent role in the design, analysis and support of large-scale numerical investigations.



**Acknowledgements** The authors would like to thank Prof. Johan Larsson for very kindly providing us with code, *Hybrid* that was used to perform the high fidelity turbulent simulation. The authors have also significantly benefited from a generous CPU allocation on Purdue's eighth on-campus supercomputer, Rice and from the fruitful discussions with the technical staff.

## References

1. N. A. Adams and K. Shariff. Conservative hybrid compact-weno schemes for shock-turbulence interaction. *J Comput Phys*, 1996.
2. Ivan Bermejo-Moreno, J. Bodart, J. Larsson, and B.M. Barney. Solving the compressible Navier-Stokes equations on up to 1.97 million cores and 4.1 trillion grid points. In *IEEE International Conference on High Performance Computing*, 2013.
3. G. A. Bres, M. Inkman, T. Colonius, and A. V. Fedorov. Second-mode attenuation and cancellation by porous coatings in a high-speed boundary layer. *J. Fluid Mech.*, 726:312, 2013.
4. G. N. Coleman, J. Kim, and R. D. Moser. A numerical study of turbulent supersonic isothermal-wall channel flow. *J. Fluid Mech.*, 305(-1):159–183, December 1995.
5. N. De Tullio and N. D. Sandham. Direct numerical simulation of breakdown to turbulence in a Mach 6 boundary layer over a porous surface. *Phys. Fluids*, 22:094105, 2010.
6. Hussaini M Y Duck P W, Erlebacher G. On the linear stability of compressible plane couette flow. *J. Fluid Mech.*, 258:131–165, 1994.
7. Vahid Esfahanian. *Computation and stability analysis of laminar flow over a blunt cone in hypersonic flow*. PhD thesis, The Ohio State University, 1991.
8. R. Friedrich and F. P. Bertolotti. Compressibility effects due to turbulent fluctuations. *Appl. Sci Res*, 57(165–194), 1997.
9. Lekoudis S. G. Stability of boundary layer over permeable surfaces. In *AIAA Aerosp. Sci. Meet. Exhibit*, Huntsville, AL 1-8, 1978.
10. S. Hu and X. Zhong. Linear instability of compressible plane couette flows. In *AIAA Aerosp. Sci. Meet. Exhibit*, pages 1–16, Reno, NV, 1997.
11. Sean Hu and Xiaolin Zhong. Linear stability of viscous supersonic plane couette flow. *Phys. Fluids*, 10(3):709 – 730, 1998.
12. P. G. Huang, G. N. Coleman, and P. Bradshaw. Compressible turbulent channel flows: DNS results and modelling. *J. Fluid Mech.*, 305(-1):185–218, December 1995.
13. J. Jiménez and A. Pinelli. The autonomous cycle of near-wall turbulence. *J. Fluid Mech.*, 389:335–359, 1999.
14. J. Jiménez, M. Uhlmann, A. Pinelli, and G. Kawahara. Turbulent shear flow over active and passive porous surfaces. *J. Fluid Mech.*, 442:89–117, September 2001.
15. J. Larsson, I. Bermejo-Moreno, and S. K. Lele. Reynolds - and mach-number effects in canonical shock-turbulence interaction. *J. Fluid Mech.*, 2013.
16. J. Larsson and S.K. Lele. Direct numerical simulation of canonical shock/turbulence interaction. *Phys. Fluids*, 12, 2009.
17. Mack L M. On the inviscid acoustic-mode instability of supersonic shear flows. *Theor. Comput. Fluid Dyn.*, 2(2):97–123, 1990.
18. M. Malik, J. Dey, and M. Alam. Linear stability, transient energy growth, and the role of viscosity stratification in compressible plane couette flow. *Phys Rev E*, 77:1–15, 2012.
19. M. L. Malik. Numerical methods for hypersonic boundary layer stability. In *J Comput Phys*, volume 86, pages 376–413, 1990.
20. S. Pirozzoli. Conservative hybrid compact-weno schemes for shock-turbulence interaction. *J. Comput. Phys.*, 178:81–117, 2002.
21. Rist U Probst A, Radespiel R. Linear-stability-based transition modeling for aerodynamic flow simulations with a near-wall reynolds-stress model. *AIAA J.*, 50(2):416–428, 2012.
22. C. Scalo, J. Bodart, and S. K. Lele. Compressible turbulent channel flow with impedance boundary conditions. *Phys. Fluids*, 27(035107), 2015.

23. C. K. W. Tam and L. Auriault. Time-domain Impedance Boundary Conditions for Computational Aeroacoustics. *AIAA J.*, 34(5):917 – 923, 1996.
24. N. Tilton and L. Cortelezzi. Linear stability analysis of pressure-driven flows in channels with porous walls. *J. Fluid Mech.*, 604:411–445, 2008.
25. A. Wagner. *Passive Hypersonic Boundary Layer Transition Control Using Ultrasonically Absorptive Carbon-Carbon Ceramic with Random Microstructure*. PhD thesis, Katholieke Universiteit, Leuven, 2014.
26. A. Wagner, K Hannemann, and M. Kuhn. Experimental investigation of hypersonic boundary-layer stabilization on a cone by means of ultrasonically absorptive carbon-carbon material. AIAA Paper 2012-5865, 2012.
27. V. Wartemann, H. Lüdeke, and N. D. Sandham. Numerical Investigation of Hypersonic Boundary-Layer Stabilization by Porous Surfaces. *AIAA J.*, 50:1281, 2012.
28. M Weder. *Linear Stability and Acoustics of a Subsonic Plane Jet Flow*. PhD thesis, ETH, Zurich, Switzerland, 2012.